Modelling of methane-air combustion on ceramic foam surface burners in the radiation mode

MODELLING OF METHANE-AIR COMBUSTION ON CERAMIC FOAM SURFACE BURNERS IN THE RADIATION MODE

P.H. Bouma, L.M.T. Somers, L.P.H. de Goey and J.K. Nieuwenhuizen
Eindhoven University of Technology
Dept. of Mechanical Engineering (WOC, WH 3.138)
PO BOX 513
5600 MB EINDHOVEN - THE NETHERLANDS

ABSTRACT

The flame behaviour of a ceramic foam surface burner in the radiation mode has been studied. Two models are presented. The first numerical model is based on the skeletal mechanism for lean methane-air combustion consisting of 25 reactions among 16 species. Surface radiation of the burner is included. The second simple analytical model is based on the known behaviour of 1D flames on an externally cooled perfectly conducting burner. The radiative heat loss of the burner is balanced with the energy loss of the flame to the burner. Both models predict the same non-adiabatic flame temperature within a few degrees. There is a slight difference between the predicted surface temperatures, which is caused by errors in the average value for the heat capacity in the second model. Results of the surface and gas temperature measurements show the same trends as the numerical computations, although the absolute values show some discrepancies. The discrepancies of the surface temperature are caused by uncertainties of the effective emissivity of the surface, and the discrepancies of the gas temperature are caused by the rather large corrections of the thermocouple temperature.

Keywords: Radiation mode, Discretization, Surface temperature, Flame temperature, Arrhenius relation.

1 INTRODUCTION

In the last decade much attention is paid to the development of fully premixed burners. The 'Netherlands Energy Research Foundation' (ECN) uses a porous ceramic foam as flame holder for its low NO emission features. Another advantage of this burner besides the low NO emission is the large range of energy modulation. In the radiation mode of the burner, the mixture velocity is less than the adiabatic burning velocity. The flame stabilizes close to or even partly inside the foam. The flame stabilizes by conductive heat loss to the ceramic foam. As a consequence, the ceramic is heated up and loses its energy by radiation. The gasflow and the combustion phenomena can assumed to be one-dimensional in this mode.

When the mixture velocity exceeds the burning velocity, Bunsen type flames appear. The flame average length is rather short ($\mathcal{O}(1cm)$) and the flames are cooled by the burner at the stabilization points only,

so that the ceramic foam will remain relatively cool. This energy modulation range is called the 'blue flame mode' due to the visible blue flames. The combustion phenomena are essentially three-dimensional in this mode.

Much research on radiant burners has been done in the last decade. However, much of the attention is paid to the combustion phenomena inside a porous medium [1], [2] and [3]. Since the material temperatures can be rather high (more than 1000^oC) inside the foam, energy transport by internal radiation has to be included. In most cases a one-step reaction mechanism is used. Hsu and Matthews [3], however, use complex chemistry. The advantage of using complex chemistry is that a more accurate prediction of temperature distribution is possible. Also the concentration profiles of the chemical species give detailed information about CO and NO-emissions.

Less information is available for surface combustion on ceramic burners. Golombok et al. [4] recently studied surface combustion using metal fibre burners. They used a one-step reaction model and included a radiation loss term at the surface. Radiation inside the burner was included by changing the effective conductivity. The effective conductivity is proportional to T^3.

Nakamura et al. [5] recently presented a model for methane combustion on the surface of a porous ceramic plate. They also used a one-step reaction model and neglected conduction of the gas mixture inside the porous foam. The flame was stabilized completely on top of the foam, which was probably caused by the low porosity of the burner ($\phi = 0.36$, whereas our foam has a porosity of $\phi \approx 0.90$).

This paper focuses at surface combustion in the radiation mode. In this mode the flame will be flat and the system can assumed to be one-dimensional. This will simplify the reaction and flow equations considerably.

In section 2 we will present the two models which are used to study the behaviour of surface combustion. In subsection 2.2 the governing equations together with the boundary conditions for the first numerical model are given. The discretized equations describing the phenomena near the outlet of the ceramic foam layer are derived in subsection 2.3. In subsection 2.4 the second, analytical model is presented. In section 3 methods of the temperature measurements of the surface and the gas are presented. The modelling results and the experimental data are compared in section 4, and in section 5 some conclusions are drawn.

2 MODELLING

2.1 Introduction

Two models for the combustion behaviour are presented. Model 1, presented in subsections 2.2 and 2.3, is based on the skeletal mechanism [6] for lean methane oxidation. The skeletal scheme consists of 25 reactions among 16 species (CH_4, CH_3, CH_3O, CH_2O, HCO, CO, CO_2, O_2, O, H_2, H, OH, HO_2, H_2O_2, H_2O and N_2). Together with the related mass conservation equations, differential equations for the temperatures of the gas and ceramic are solved.

Model 2, presented in subsection 2.4, is an analytical model based on approximations of the equations for the flame and the ceramic foam. An Arrhenius type of equation [7] is used to calculate the relation between the mass flow rate and the non-adiabatic flame temperature. In steady-state the energy flux between flame and ceramic is balanced with the radiation heat loss of the ceramic surface. Quick estimates of the flame and

surface temperature can be made with this model.

2.2 Governing equations

The combustion system is controlled by the convection-diffusion-reaction equations for the chemical species and the enthalpy balance equations for the reacting gas mixture and the ceramic foam. The convection-diffusion-reaction equations are given by:

$$\phi\rho_g\frac{\partial Y_i}{\partial t}+\rho_g u\frac{\partial Y_i}{\partial x}-\frac{\partial}{\partial x}\left(\phi\rho_g D_{im}\frac{\partial Y_i}{\partial x}\right)=\phi\dot{\rho}_i \quad \text{with} \quad i\in[1,16] \tag{1}$$

where Y_i, ρ_g and $\dot{\rho}_i$ represent the mass-fraction, the mass density and the chemical source term of species i, respectively. The gas velocity, the position and time are represented by u, x and t. The diffusion coefficient D_{im} of species i in the mixture m is temperature and composition dependent. The porosity ϕ equals one outside the foam and is approximately equal to 0.9 inside the foam. Note that the gas volume is reduced by a factor ϕ inside the foam. Consequently the velocity u is increased by a factor $1/\phi$, so that the massflux $\dot{m}=\rho_g u$ remains equal inside and outside the foam when the stationary system is considered.

The enthalpy balance equation for the gas is given by:

$$\begin{aligned}\phi\rho_g c_{p,g}\frac{\partial T_g}{\partial t}+\rho_g u c_{p,g}\frac{\partial T_g}{\partial x} \quad &- \quad \frac{\partial}{\partial x}\left(\phi\lambda_g\frac{\partial T_g}{\partial x}\right) \\ &= \quad \alpha A(T_s-T_g)-\phi\sum_{i=1}^{N}h_i\dot{\rho}_i-\phi\sum_{i=1}^{N}\rho_g Y_i c_{p,i}U_i\frac{\partial T_g}{\partial x}.\end{aligned} \tag{2}$$

The terms on the left-hand side represent the instationairy, the convective and conductive heat transport. Both the heat capacity $c_{p,g}$ as the heat conductivity λ_g are temperature and mixture dependent.

The first term on the right-hand side represents the heat transfer between the gas and the solid. The product of the heat transfer coefficient α and the specific surface A determines the coupling between the ceramic foam temperature T_s and the gas temperature T_g. This term is the only coupling between the gas and the ceramic and is an important parameter for the flame stabilization process. The second term describes the total heat release due to chemical reactions, where h_i represents the enthalpy of species i. The third term on the right-hand side stands for the enthalpy transport due to diffusive fluxes. This term is generally small [6] and is therefore neglected.

The equation for the ceramic temperature is given by:

$$(1-\phi)\rho_s c_{p,s}\frac{\partial T_s}{\partial t}-\frac{\partial}{\partial x}\left((1-\phi)\lambda_s\frac{\partial T_s}{\partial x}\right)=-\alpha A(T_s-T_g), \tag{3}$$

where ρ_s, $c_{p,s}$ and λ_s represent the mass density, the heat capacity and the conductivity of the bulk material of the ceramic foam. The terms in the ceramic temperature equation represent the variations of temperature in time, the conduction of heat and the heat transfer between gas and solid.

The set of equations is closed with the ideal gas law and the continuity relation

$$P_0=\frac{\rho_g R T_g}{\bar{M}} \tag{4}$$

and

$$\phi\frac{\partial\rho_g}{\partial t}+\frac{\partial\rho_g u}{\partial x}=0, \tag{5}$$

with R the universal gas constant. The pressure P_0 is approximate constant for deflagrations processes (low Mach numbers). The average molar mass $\bar{M}$ is given by:

$$\bar{M} = \left[\sum_{i=1}^{N} \frac{Y_i}{M_i} \right]^{-1}. \tag{6}$$

We will consider the stationary system, so the massflux $\dot{m} = \rho_g u$ is constant and the time dependent terms of Eqs. (1), (3), (3) and (5) are zero.

The computational domain, shown in figure 1, is divided into three zones: an unburnt gas zone, a ceramic/gas zone and a flame zone. The gas temperature T_g and the mass-fractions of species N_2, O_2 and CH_4 are fixed at the inflow of the computational domain. We use zero-flux boundary conditions for the other species at the inflow. At the outflow we use zero-flux boundary conditions for all the species and the gas temperature.

The boundary condition of the differential equation for the ceramic temperature at the inlet ($x = -L$) and outlet ($x = 0$) of the ceramic foam layer are found by integrating the differential equation around the inlet or outlet from $-\delta$ to $+\delta$ with δ approximating to zero. The boundary condition for Eq. (3) at the outlet then yields:

$$-(1-\phi)\lambda_s \left. \frac{\partial T_s}{\partial x} \right|_{x \uparrow 0} = q_{rad}. \tag{7}$$

The energy loss by radiation at the surface is represented by q_{rad}:

$$q_{rad} = \bar{\epsilon}\sigma(T_{surf}^4 - T_{surr}^4), \tag{8}$$

with $\bar{\epsilon}$ the effective emissivity of the surface, σ the Stefan-Boltzmann constant and $T_{surf} = T_s(x = 0)$, the temperature of the ceramic foam at the outlet surface. The temperature T_{surr} is the temperature of the surroundings, and is chosen to be equal to the cold unburnt gas temperature T_0 for a burner in an open atmosphere. The boundary and step conditions at the inlet of the foam are similar and can be derived analogously. Note that at the inlet the difference between the surroundings and the ceramic temperature in most cases (when $L = \mathcal{O}(1cm)$) is only a few degrees, so that radiation at the inlet can be neglected.

2.3 Discretization method

The computational domain (see figure 1) runs from $x = -2cm$ to $x = 8cm$ and is divided in control volumes. The control volume used is shown in figure 2. The known conservative finite-volume discretization method of Thiart [8] is used to discretize the equations for the mass fractions and energy equations in these control volumes (see appendix A). An adaptive locally refined gridding technique [9] is used to resolve the large gradients in the preheat and the reaction zones.

The discretized energy equations at the interfaces of the ceramic foam at $x = -L$ and $x = 0$ demand special attention. This is treated in this subsection. The implementation of radiation at the surfaces is slightly different from the method used by Beckermann and Smith [10]. They implement the radiating surface at the interface between the control volumes, while we implement the surface at a gridpoint to be able to use adaptive gridding strategies without limitations.

We will define three flux functions J. The convective and diffusive fluxes of Eq. (1) are combined in the mass-flux term J_i of species i:

$$J_i = \rho_g u Y_i - \phi \rho_g D_{im} \frac{\partial Y_i}{\partial x}. \tag{9}$$

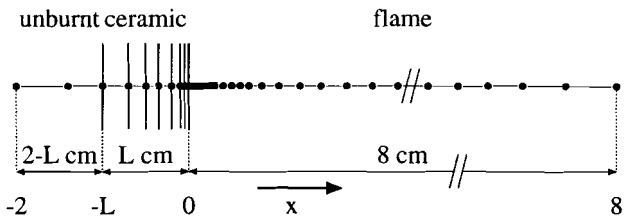

Figure 1: Computational domain.

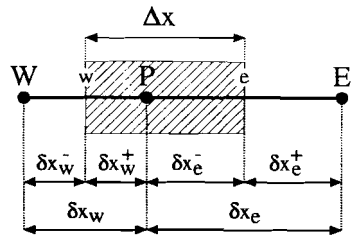

Figure 2: Control volume.

The heat-flux J_g of the gas is given by:

$$J_g = \rho_g u T_g - \frac{\phi \lambda_g}{c_{p,g}} \frac{\partial T_g}{\partial x}, \tag{10}$$

and the heat-flux J_s of the solid temperature is defined as:

$$J_s = \frac{(1-\phi)\lambda_s}{c_{p,s}} \frac{\partial T_s}{\partial x}. \tag{11}$$

With the nomenclature defined in figure 2 we can integrate Eqs. (1), (3) and (3) from $-\delta x_w^+$ to δx_e^- over the control volume around the point P. The source terms $\phi \dot{\rho}_i$, $\frac{\alpha A}{c_{p,g}}(T_s - T_g)$, $\frac{\alpha A}{c_{p,s}}(T_s - T_g)$ and $\frac{\phi}{c_{p,g}} \sum_{i=1}^{N} h_i \dot{\rho}_i$ are assumed to be constant inside the control volume. The values of the source terms S are chosen at the midpoint P. The diffusivities $\phi \rho_g D_{im}$, $\frac{\phi \lambda_g}{c_{p,g}}$ and $\frac{(1-\phi)\lambda_s}{c_{p,s}}$ are assumed to be constant between the gridpoints. Assume that the diffusivity and the source terms are constant in an interval $[0, L]$. Then the exact solution of the differential equations at x in the interval $[0, L]$ is:

$$F(x) = F_0 + \frac{Sx}{\rho u} + \frac{F_L - F_0 - (SL/\rho u)}{exp(\rho u L/\Gamma) - 1} \left[exp\left(\frac{\rho u x}{\Gamma}\right) - 1 \right], \tag{12}$$

where Γ denotes the general diffusivity and F the general observable (Y_i, T_g or T_s). The general flux J is now given by:

$$J = \rho u F - \Gamma \frac{\partial F}{\partial x}, \tag{13}$$

and the integrated convection-diffusion equations then yield:

$$J^e - J^w - \Delta x S = 0, \tag{14}$$

with J^w the flux at the inflow of the control volume and J^e the flux at the outflow of the control volume. The values of the fluxes are obtained by using the exact solution for constant S and Γ between the gridpoints. The discretized east-flux J^e is then given by:

$$J^e = \rho u \left[F^P + \frac{F^P - F^E}{exp(\rho u \delta x_e^- / \Gamma) - 1} \right] + S \left[\delta x_e^- - \frac{\Gamma}{\rho u} + \frac{\delta x_e}{exp(\rho u \delta x_e^- / \Gamma) - 1} \right], \tag{15}$$

with F^P and F^E the values of the observable at the midpoint and east-point respectively. A similar equation can be obtained for the flux at the west-side of the control volume.

The Eqs. (1), (3) and (3) at the outlet interface of the ceramic foam can now be discretized. The integration of the convection-diffusion-reaction equation now yields:

$$J_i^e - J_i^w - (\phi \delta x_w^+ + \delta x_e^-)\dot{\rho}_i = 0. \tag{16}$$

The discretized fluxes J_i^e and J_i^w are given in appendix A. Note that at the west-side the porosity $\phi \approx 0.9$, which has to be multiplied with the source function $\dot{\rho}$.

The enthalpy equations are more complicated, since the heat transfer is not constant in the entire control volume. Also the radiation term in the ceramic enthalpy equation has to be included at the midpoint P.

The heat transfer is non-zero on the west-side and zero at the east-side (at the burner inlet it is the other way around). The averaged temperatures of gas and ceramic in the control volume are not the temperatures at the midpoint, as would be if the control volume lies in the ceramic zone, but at $-1/2\delta_w^+$. This states that the heat transfer source term is altered:

$$(\delta x_w^+ + \delta x_e^-)\alpha A \left(T_s^P - T_g^P\right) \Longrightarrow \delta x_w^+ \alpha A \left(\frac{3T_s^W + T_s^P}{4} - \frac{3T_g^W + T_g^P}{4}\right), \tag{17}$$

where we have assumed that the temperature is linear between the midpoint P and the westpoint W.

The discretized versions of Eqs. (3) and (3) at the outlet are now given:

$$J_g^e - J_g^w - (\phi \delta x_w^+ + \delta x_e^-)\sum_{i=1}^{N} h_i \dot{\rho}_i - \delta x_w^+ \alpha A \left(\frac{3T_s^W + T_s^P}{4} - \frac{3T_g^W + T_g^P}{4}\right) = 0, \tag{18}$$

and

$$J_s^w - \delta x_w^+ \alpha A \left(\frac{3T_s^W + T_s^P}{4} - \frac{3T_g^W + T_g^P}{4}\right) - q_{rad}(T_s^P) = 0, \tag{19}$$

with

$$J_s^w = \frac{(1-\phi)\lambda_s}{c_{p,s}} \frac{T_s^P - T_s^W}{\delta x_w}. \tag{20}$$

The fluxes J_g^e and J_g^w are given in appendix A. The discretized relations at the inlet are similar.

The discretized set of equations has to be solved by numerical techniques. At every point we have N equations, so we have $N \times K$ equations, where K is the total number of gridpoints. The set of equations is linearized by using a modified Newton-Raphson technique [9]. The linearized set of equations can now be written as a matrix equation $\mathbf{Ax} = \mathbf{b}$ with $\mathbf{A}$ having a block tri-diagonal structure. This set is solved by standard techniques.

2.4 Analytical model

It appears that for many applications the final gas temperature and the surface temperature are of interest and that the concentration of the chemical species is of minor importance. In these cases it would be useful if simple analytical relations would be available to obtain these temperatures. In the sixties Kaskan [7] measured relations between the mass burning velocity u and the non-adiabatic flame temperature T_b' for flames stabilized on a water-cooled surface burner. For methane combustion he obtained an Arrhenius like equation between temperature and mass burning velocity:

$$u = k e^{-E_a/2RT_b'}, \tag{21}$$

with k a constant and E_a the overall activation energy. The constant k of Eq. (21) can be eliminated when the adiabatic flame temperature T_b and the adiabatic burning velocity s_L are known. One obtains:

$$T_b' = \left(\frac{1}{T_b} - \frac{2R}{E_a} ln \frac{u}{s_L} \right)^{-1}. \tag{22}$$

It can be shown easily [11] that this relation is also valid for other cooling-stabilized burners, when the reaction zone is not in contact with the heat absorbing material. It remains to be seen whether this is true for the ceramic burner, where part of he reactions take place inside the material.

In table 1 the overall activation energies, the adiabatic flame temperature T_b and the adiabatic burning velocity s_L of atmospheric methane combustion with air are given.

table 1: Methane combustion. [7] and [12]

$1/n$	$E_a[J]$	$T_b[K]$	$s_L[cm/s]$	$1/n$	$E_a[J]$	$T_b[K]$	$s_L[cm/s]$
1.20	305	2136	34.6	0.95		2172	34.6
1.15		2173	37.2	0.90		2120	32.1
1.10		2210	38.3	0.85		2057	28.0
1.05		2228	38.3	0.80	234	1993	23.9
1.00	272	2220	36.7	0.75		1912	19.4

The flame is cooled by the ceramic foam when the gas velocity is lower than the adiabatic burning velocity. The enthalpy loss Δq of the flame is given by:

$$\Delta q = \rho_g u c_{p,g} (T_b - T_b'). \tag{23}$$

The flame can only stabilize when the enthalpy loss of the flame is in balance with the enthalpy loss of the burner due to radiation given by Eq. (8). When the Eqs. (8), (22) and (23) are combined, one obtains a relation between the surface temperature and the gas velocity:

$$T_{surf}^4 = T_0^4 + \frac{\rho_g u c_{p,g} T_b}{\bar{\epsilon}\sigma} \frac{2RT_b ln\left(\frac{u}{s_L}\right)}{2RT_b ln\left(\frac{u}{s_L}\right) - E_a}. \tag{24}$$

As indicated, this method can be used only when the reaction zone is essentially outside the burner. The real flame temperature will be lower than the temperature predicted by Eq. (22) when the latter is not the case. The cooling effect by the foam will be larger when the flame lies inside the foam, since the flame loses energy to the foam in and after the reaction zone. The effective conductivity is also changed when the flame zone lies inside the ceramic foam. This will lead to an increase of the burning velocity [1].

3 EXPERIMENTS

Temperature measurements of the outlet interface of the ceramic burner and the flame have been performed at the 'ECN' and at the 'TUE'. The surface temperature is measured with two types of pyrometers and with a pyrolaser. The main problem we had to deal with is the presence of gas radiation. At a relatively low load gas radiation is negligible compared to surface radiation, but at higher loads this is not the case. We measured

the surface radiation intensity at several wavelengths: $0.865\mu m$ (pyrolaser), $0.96\mu m$ and $3.8\mu m$ (pyrometers). At a wavelength of $3.8\mu m$ the measurements are not obscured by gas radiation, but at the other wavelengths it is. This means that at a relatively high load, where the influence of surface radiation is lower, the measured surface temperature is systematically too high.

Furthermore we have to keep in mind that the emissivity of the surface is temperature and wavelength dependent. Therefore we have to estimate a mean emissivity, which can be adjusted on the pyrometers. The pyrolaser measures the radiant intensity and the reflectivity at a wavelength of $0.865\mu m$. The emissivity is obtained by subtracting the reflectivity from one. Here it is assumed that transmission of the foam is zero. Note that the obtained emissivity can differ from the mean emissivity, since the mean radiation contribution is in the infrared ($2.6\mu m$), while the emissivity is measured in the low-infrared (close to the visible region). This again is an error source which can not be neglected. If for instaance the mean emissivity $\bar{\epsilon}$ equals 0.6 instead of 0.4, then the error is $\mathcal{O}(10^2)K$.

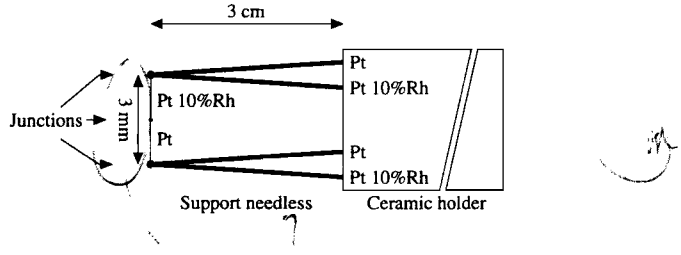

Figure 3: Triple thermocouple

The flame temperature is measured with a so-called triple thermocouple [12] shown in figure 3. The measurement device consists of three couples, two at the support needles and one junction in the center as usual. The middle thermocouple wires have a diameter of $50\mu m$ and the wires of the support needles a diameter of $500\mu m$. The measured temperature at the middle junction is corrected for radiation and conduction. The correction can be performed by solving the differential energy balance equation of the couple:

$$\alpha_c[T_b' - T_c] - \sigma\epsilon_c\left(T_c^4 - T_{surr}^4\right) + \frac{1}{4}d_c\lambda_c\frac{d^2T_c}{dx^2} = 0, \tag{25}$$

with T_c the temperature of the middle junction, α_c the heat transfer between gas and the thermocouple, x the position on the wire and d_c the diameter of the wires of the middle thermocouple. The boundary conditions for the second derivative are determined by the two temperatures at the support couples. The lowest-order approximation for the flame temperature is given by:

$$T_b' = T_c + \frac{\epsilon_c\sigma}{\alpha_c}\left(T_c^4 - T_{surr}^4\right) - \frac{d_c\lambda_c}{4\alpha_c}\left(\frac{T_{c,-1} - 2T_{c,0} + T_{c,1}}{(\Delta x)^2}\right), \tag{26}$$

with $T_{c,\pm1}$ the measured temperatures at the support couples and $\Delta x = 1.5mm$ the distance between the middle junction and the support junctions. The error ε in the gas temperature of the lowest-order approximation is given by:

$$\varepsilon(T_b') = \mathcal{O}\left(\frac{d_c\lambda_c\Delta x\frac{\partial^4T_c}{\partial x^4}}{4\alpha_c}\right) = \mathcal{O}(0.3 \times \Delta T_c)K, \tag{27}$$

which can be rather large, since the temperature difference between middle junction and support junctions can be $\mathcal{O}(200)K$.

4 RESULTS

The modelling and experimental results are discussed in this section. First, the flame behaviour predicted by model one is compared with the numerically computed flame behaviour of a perfectly cooled burner stabilized flame. The results of the temperatures of model one and model two are discussed subsequentially. Finally, the results of the temperature measurements are compared with the numerical results.

In the figures 4 and 5 temperature profiles are shown for a typical flame with airratio $n = 1.25$. The numerical code which is used to compute the cooled burner stabilized flame (fig. 5) is essentially the same as the code we use to compute the flame behaviour of the ceramic foam burner (fig. 4). The only difference between both configurations is the numerical treatment of the burner temperature. The temperature of the ceramic burner is dictated by the energy balance and the surface radiation, while the temperature of the externally cooled burner is modelled with a constant temperature of $298K$.

The temperature profile of the ceramic foam is almost the same as the profile of the gas temperature in the foam as shown in figure 4. Only near the outlet there is a difference in the temperature profiles. There, the gas temperature exceeds the ceramic temperature with several hundred degrees Kelvin. The magnitude of this effect strongly depends on the value of αA. Further more, the slope of the ceramic temperature profile is negative near the outlet as indicated by the boundary condition given by Eq. (7).

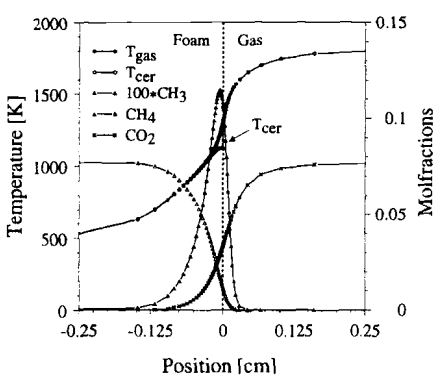

Figure 4: Concentration and temperature profiles near the outlet of the ECN burner. Airratio: 1.25; Massflow rate: $0.0150 gcm^{-2}s^{-1}$.

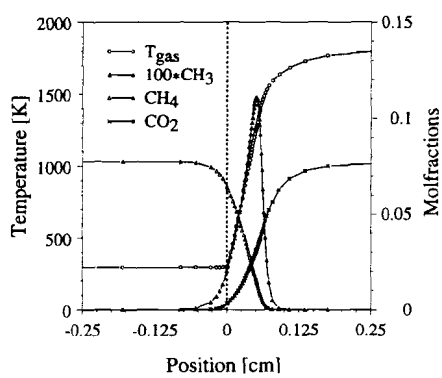

Figure 5: Concentration and temperature profiles of a stabilized flame on an externally cooled burner. Airratio: 1.25; Massflow rate: $0.0150 gcm^{-2}s^{-1}$.

The concentration profiles of CH_4, CH_3 and CO_2 are also shown in the figures 4 and 5. As shown in figure 4, the methane conversion starts inside the ceramic foam. When we compare this with a flame, which is stabilized on an externally cooled burner, as shown in figure 5, we see that the reactions take place outside the burner. Changes of concentrations of the species inside the cooled burner are caused by diffusion only. We see also a difference in the concentration profiles of the CH_3 radical. The CH_3 peak shows a broadening inside the ceramic foam compared to the cooled burner stabilized flame. This indicates that the reaction and the preheating zones are broadened within the ceramic foam. This effect is partly caused by the increasing energy transport inside the foam due to the conductivity of the foam. The change of the porosity will decrease the diffusivity of species inside the foam by a factor of ϕ, while the effective conductivity is increased. The Lewis number ($Le = \frac{\lambda_g}{\rho_g c_{p,g} D_{im}}$) will therefore increase.

Although the reactions take partly place inside the foam, the influence on the final flame temperature is marginal. The final flame temperatures differ slightly (a few K) due to the increasing energy transport in the material (see also subsection 2.4). The effect is remarkable, since this indicates that the presence of the foam does not affect the reaction zone considerably when the flame is near the outlet. Note however, that the latter effect is increased when the porosity is decreased. The temperature difference is $\mathcal{O}(5)K$ at low mass flow rates ($0.01 g\, cm^{-2}\, s^{-1}$) and less than $1K$ near blow-off. In figure 6 the results of both models mentioned in section 2 are presented. The computed flame temperatures differ no more than a few degrees. Also the

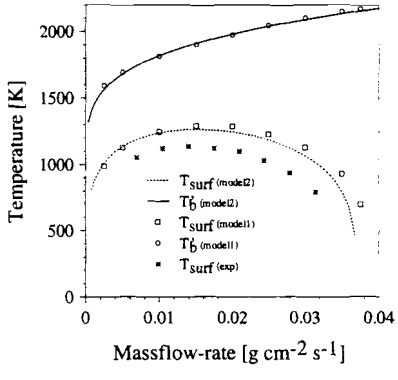

Figure 6: Flame T_b' and surface $T_{surf} = T_s(x = 0)$ temperatures computed with both models and the surface temperature measured with the pyrometer. Airratio: $n = 1.10$

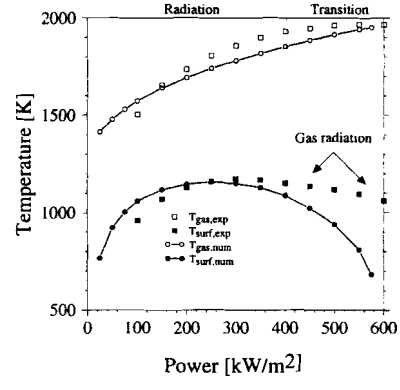

Figure 7: Flame T_b' and surface $T_{surf} = T_s(x = 0)$ temperatures computed with the numerical code, the flame temperature measured with the triple thermocouple and the surface temperature measured with the pyrolaser. Airratio: $n = 1.30$

surface temperatures show the same behaviour, which clearly indicates the validity of the second analytical model. The differences of the surface temperatures are caused by the error in the specific heat capacity. For the second model we did choose a mean specific heat capacity to speed up the calculation time, and for the complex

model the specific heat capacity is temperature dependent and mixture averaged. The minor differences in the predicted flame temperatures are probably caused by uncertainties in the constants E_a, k, T_b and s_L.

The results of the flame temperature computed with the second model compared with the results of model one indicates that the foam has no significant influence on the reaction zone. These results support the earlier conclusion which was drawn when we compared the cooled burner stabilized flame with a flame stabilized on the foam. Model two can thus be used to calculate the flame and surface temperatures when no information about species concentrations is required.

The results of the temperature measurements of the surface with the $3.8\mu m$ pyrometer are shown also in figure 6. The predicted trends of the surface temperature measurements, shown in figure 6, are correct, but the absolute values are overestimated by the models. This is probably caused by the chosen effective emissivity in the model and the adjusted emissivity of the pyrometer ($3.8\mu m$). We used an effective emissivity of 0.4, but experiments indicate that the effective emissivity, averaged over the total spectral range, is probably larger. A larger emissivity in the model would lead to lower surface temperatures, and thus giving better agreement with the experiments. However, this has to be investigated in the future.

In figure 7 the results of the flame temperature (triple thermocouple) and the surface temperature (pyrolaser) together with the data computed with model one are shown. With the pyrolaser we measured an emissivity of 0.36 at a wavelength of $0.865\mu m$. This value of the emissivity is used as input for the numerical code. In the radiation mode (to a maximum power of $400kW/m^2$) the agreement between predicted and measured surface temperature is fair. However, we have to emphasize that we measured the emissivity and the radiation intensity at a specific wavelength, and assumed that the difference between the effective emissivity and the measured emissivity is marginal. This can lead to errors of $\mathcal{O}(10^2)K$ as mentioned earlier in section 3. At higher loads, in the transition and blue flame mode, the measured radiation intensity was too high due to gas radiation, as mentioned before. However, this effect lies beyond the scope of this study.

The profiles of the computional and experimental flame temperature results have the same trend. However, the discrepancies of the absolute values of the flame temperatures are quite large. The error of the experimental flame temperature given by Eq. (27) approximates $\mathcal{O}(100)K$. The radiation correction is also slightly overestimated, since the thermocouple sees a part of the radiating surface of the burner. This can lead to an additional error of approximately $\mathcal{O}(10)K$. Catalytical reactions can also give an overestimation of the measured temperature, but we measured several millimetres above the reaction zone to minimize this effect.

5 CONCLUSIONS AND FUTURE WORK

From the results we may conclude that both models predict the flame and surface temperature profiles as a function of load and airratio with satisfactory accuracy. The temperature of the gas and surface can be obtained simply and accurately with the second analytical model. If information about the mass fractions of the species is required, then the first numerical model has to be used.

The discrepancies between the numerical and experimental flame temperature lie within the experimental error of $\mathcal{O}(100)K$. This error of the gas temperature can be decreased if the construction of the triple thermocouple is improved.

The errors of the surface temperature have several origins. First, the effective emissivity may differ with the spectral emissivity. Secondly, gas radiation cannot be neglected at higher temperatures for the pyrolaser and the $0.96\mu m$ pyrometer. For the $3.8\mu m$ pyrometer gas radiation can be ignored, since at a wavelength of $3.8\mu m$ there is no gas radiation of H_2O and CO_2 expected.

The physical features of the ceramic foam (α, λ_s, $c_{p,s}$ and ρ_s) are chosen to be temperature independent. Altering the values of these constants didn't change the flame and surface temperature significantly. The heat capacity and the mass density of the ceramic foam have influence on the convergence speed of the code, but not on the final solution. The conductivity has influence on the temperature profile inside the foam. When we did choose an unrealistic large conductivity the surface temperature was decreased. The inlet surface temperature, however, was increased to maintain the energy conservation.

The effective heat transfer parameter αA we used is rather high. This seems to be necessary to prevent flash-back or transition of surface combustion to internal combustion. These phenomena will be investigated soon.

ACKNOWLEDGEMENT

The support of ECN and NOVEM, The Netherlands, is gratefully acknowledged.

A Discretized equations in the gas and ceramic zones

The integrated differential equations of the species and enthalpy equations definied by Eqs. (1), (3) and (3) for the gas and ceramic zone are given below.

Species:
$$J_i^e - J_i^w - \Delta x \phi \dot{\rho}_i = 0, \tag{28}$$

gas:
$$J_g^e - J_g^w - \Delta x \phi \sum_{i=1}^{N} h_i \dot{\rho}_i - \Delta x \alpha A \left(T_{s,k} - T_{g,k}\right) = 0 \tag{29}$$

and ceramic:
$$J_s^w - J_s^e - \Delta x \alpha A \left(T_{s,k} - T_{g,k}\right) = 0, \tag{30}$$

where $\phi = 1$ and $\alpha A = 0$ in the gas zone and $\phi \neq 1$ and $\alpha A \neq 0$ in the ceramic zone. The discretized fluxes of the species are:

$$J_i^e = \rho_g u \left[Y_i^P + \frac{Y_i^P - Y_i^E}{exp(u\delta x_e^- / \phi D_{im}) - 1} \right] + \phi \dot{\rho}_i \left[\delta x_e^- - \frac{\phi D_{im}}{u} + \frac{\delta x_e}{exp(u\delta x_e^- / \phi D_{im}) - 1} \right] \tag{31}$$

and

$$J_i^w = \rho_g u \left[Y_i^W + \frac{Y_i^W - Y_i^P}{exp(u\delta x_w^+ / \phi D_{im}) - 1} \right] + \phi \dot{\rho}_i \left[\delta x_w^+ - \frac{\phi D_{im}}{u} + \frac{\delta x_w}{exp(u\delta x_w^+ / \phi D_{im}) - 1} \right]. \tag{32}$$

The fluxes of the gas temperature are:

$$J_g^e = \rho_g u \left[T_g^P + \frac{T_g^P - T_g^E}{exp(\rho_g u c_{p,g} \delta x_e^- / \phi \lambda_g) - 1} \right] + \frac{\phi}{c_{p,g}} \sum_{i=1}^{N} h_i \dot{\rho}_i \left[\delta x_e^- - \frac{\phi \lambda_g}{\rho_g u c_{p,g}} + \frac{\delta x_e}{exp(\rho_g u c_{p,g} \delta x_e^- / \phi \lambda_g) - 1} \right] \tag{33}$$

and

$$J_g^w = \rho_g u \left[T_g^W + \frac{T_g^W - T_g^P}{exp(\rho_g u c_{p,g} \delta x_w^+ / \phi \lambda_g) - 1} \right] + \frac{\phi}{c_{p,g}} \sum_{i=1}^{N} h_i \dot{\rho}_i \left[\delta x_w^+ - \frac{\phi \lambda_g}{\rho_g u c_{p,g}} + \frac{\delta x_w}{exp(\rho_g u c_{p,g} \delta x_w^+ / \phi \lambda_g) - 1} \right]. \tag{34}$$

The ceramic fluxes are:

$$J_s^e = \frac{1-\phi}{c_{p,s}} \frac{T_s^E - T_s^P}{\delta x_e} \tag{35}$$

and

$$J_s^w = \frac{1-\phi}{c_{p,s}} \frac{T_s^P - T_s^W}{\delta x_w} \tag{36}$$

NOMENCLATURE

Roman symbols

A	specific area	(cm^2/cm^3)			
c_p	specific heat	$(J/g\,K)$	n	airratio	$(-)$
d	diameter	(cm)	P	pressure	(Pa)
D	diffusion coefficient	(cm^2/s)	q	heat flux density	(W/m^2)
E_a	activation energy	(J/mol)	R	universal gasconstant	$(J/mol\,K)$
F	observable	(different units)	S	source function	(different units)
h	formation enthalpy	(J/g)	s_L	burning velocity	(cm/s)
J	flux	(different units)	T	temperature	(K)
k	Arrhenius constant	(cm/s)	t	time	(s)
L	thickness of the burner	(cm)	u	velocity	(cm/s)
$\bar{M}$	average molar mass	(g/mol)	U	diffusion velocity	(cm/s)
M	molar mass	(g/mol)	x	position	(cm)
$\dot{m}$	total mass flow rate	$(g/cm^2\,s)$	Y	mass fraction	$(-)$

Greek symbols

α	coefficient of transmission	$(W/cm^2\,K)$	λ	coefficient of conduction	$(W/cm\,K)$
Δ	difference	$(-)$	ϕ	porosity	$(-)$
$\bar{\epsilon}$	effective emissivity	$(-)$	ρ	density	(g/cm^3)
ε	error	(K)	$\dot{\rho}$	chemical source term	$(g/cm^3\,s)$
Γ	diffusivity	(different units)	σ	constant of Boltzmann	$(W/cm^2\,K^4)$

Indices

a	activation	P	midpoint
b	burning	rad	radiation
c	thermocouple	s	solid burner material
E	east-point	$surf$	surface of the burner plate
e	east	$surr$	surroundings
g	gas	W	west-point
i	species number	w	west
L	laminar	0	normal conditions

References

[1] Sathe, S.B., Peck, R.E. and Tong, T.W., Flame Stabilization and Multimode Heat Transfer in Inert Porous Media: A Numerical Study, *Combustion Science and Technology*, vol. 70, pp. 93-109, 1990.

[2] Sathe, S.B., Peck, R.E. and Tong, T.W., A numerical analysis of combustion and heat transfer in porous radiant burners, *ASME HTD* vol. 6, pp. 642-648, 1989.

[3] Hsu, P and Matthews, R.D., The Necessity of Using Detailed Kinetics in Models for Premixed Combustion Within Porous Media, *Combustion and Flames*, vol. 93, pp 457-466, 1993.

[4] Golombok, M., Prothero, A., Shirvill, L.C. and Small, L.M., Surface Combustion in Metal Fibre Burners, *Combustion Science and Technology*, vol. 77, pp. 203-223, 1991.

[5] Nakamura, Y., Itaya, Y., Miyoshi, K. and Hasatani, M., Mechanism of Methane-Air Combustion on the Surface of a Porous Ceramic Plate, *Journal of Chemical Engineering of Japan*, vol. 26 no. 2, pp. 205-211, 1993.

[6] Smooke, M.B., Reduced Kinetics Mechanisms and Asymptotic Approximations for Methane-Air Flames, *Lecture Notes in Physics, 384*, Springer Verlag, 1991 (ISBN 3-540-54210-8).

[7] Kaskan, W.E., The Dependence of Flame Temperature on Mass Burning Velocity, *Sixth Symposium (International) on Combustion, The Combustion Institute*; pp. 134-143, 1967.

[8] Thiart, G.D., Finite Difference Scheme for the Numerical Solution of Fluid Flow and Heat Transfer Problems on Nonstaggered Grids, *Numerical Heat Transfer*, Part B. vol. 17, pp. 43-62, 1990.

[9] Somers, L.M.T., The simulation of flat flames with detailed and reduced chemical models, *Ph.D. Thesis Eindhoven University*, 1994.

[10] Beckermann, C. and Smith, T.F., Incorporation of Internal Surface Radiant Exchange in the Finite-volume Method, *Numerical Heat Transfer, Part B*, vol. 23, pp. 127-133, 1993.

[11] de Goey, L.P.H., van Maaren, A. and Quax, R.M., Stabilization of Adiabatic Premixed Laminar Flames on a Flat Flame Burner, *Combustion Science and Technology*, vol. 92, pp. 201-207, 1993.

[12] van Maaren, A., One-step chemical reaction parameters for premixed laminar flames, *Ph.D. Thesis Eindhoven University*, 1994.